Geomagnetic Deviation of Relativistic Electron Beams Producing Terrestrial Gamma Ray Flashes

Sebastien Celestin, Nini L. Berge, Bagrat G. Mailyan, Michael S. Briggs

AGU
ADVANCING
EARTH AND
SPACE SCIENCE

JGR Space Physics

Key Points:
- Statistically significant excess of TGFs is detected to the east of their presumed sources by Fermi
- This is consistent with the expected geomagnetic field effect on relativistic runaway electron beams
- The discovered excess can be used to estimate the *E*-field in TGF source regions, which is found close to or larger than the RREA threshold

Correspondence to:
S. Celestin,
sebastien.celestin@cnrs-orleans.fr

Geomagnetic Deviation of Relativistic Electron Beams Producing Terrestrial Gamma Ray Flashes

Sebastien Celestin[1] , **Nini L. Berge[1]** , **Bagrat G. Mailyan[2]** , and **Michael S. Briggs[2,3]**

[1]LPC2E, University of Orleans, CNRS, Orleans, France, [2]Center for Space Plasma and Aeronomic Research, University of Alabama in Huntsville, Huntsville, AL, USA, [3]Department of Space Science, University of Alabama in Huntsville, Huntsville, AL, USA

Abstract In this work, we investigate the effect of the geomagnetic field on terrestrial gamma ray flashes (TGFs). Although this effect should be relatively weak for a single event, for example compared to the effect of the electric field orientation in the source region, it must be systematically present. Indeed, we show that a statistically significant excess of TGFs is detected to the east of their presumed lightning source by Fermi-Gamma-ray Burst Monitor (GBM). The corresponding eastward deviation is found to be likely greater than 0.1° in longitude, which is consistent with the expected effect of the geomagnetic field on relativistic runaway electron beams producing TGFs. Using analytical and numerical means, we show that the geomagnetic deviation can be used to estimate the magnitude of the electric field in TGF source regions. The electric field magnitudes we obtain are consistent with those necessary to drive relativistic runaway electron avalanches (RREAs).

1. Introduction

Terrestrial gamma ray flashes (TGFs) are submillisecond bursts of high-energy photons produced during the acceleration of relativistic electrons in thunderstorms (e.g., Dwyer et al., 2012). Since their discovery by Fishman et al. (1994), they have been mostly detected by spaceborne instruments (Briggs et al., 2010; Marisaldi et al., 2010; Smith et al., 2005). TGFs are believed to be produced deep inside the atmosphere at altitudes typically ranging from 10 to 15 km, and are associated with initial stages of the propagation of ascending intracloud (+IC) negative leaders (e.g., Cummer et al., 2011, 2014, 2015; Lu et al., 2010; Mailyan et al., 2018; Pu et al., 2019; Stanley et al., 2006; Xu et al., 2012).

Published models differ about the mechanisms leading to the production of energetic seed electrons and the exact context in which electric fields responsible for the acceleration of electrons arise, but there is a consensus that the mechanism of relativistic runaway electron avalanches (RREAs) is essential to explain many TGFs observed by satellites (e.g., Dwyer & Smith, 2005; Dwyer et al., 2012). There exists an energy beyond which the probability of electron collisions, and especially ionizing collisions, decreases as the electron energy increases. This probability can become sufficiently low so that electrons gain more energy from an electric field than that they lose through collisions. Such electrons are named runaway electrons. Runaway electrons still knock other electrons off air molecules with a given energy-dependent probability per unit time or per unit length, most of these secondary electrons being in low-energy range and rapidly thermalized. On rare occasions, secondary electrons will have a sufficient energy to become runaway electrons themselves. This avalanche process, the so-called RREA, is associated with a spectral signature, namely, a ∼7 MeV exponential cutoff, that is transferred to the related bremsstrahlung emission and is observed in many TGFs (e.g., Dwyer & Smith, 2005; Mailyan et al., 2016, 2019).

Theoretical models vary in the role they give lightning leaders in seeding high-energy electrons and in the way they increase the electric field in the TGF source region. In relativistic-feedback-based models, multiple RREAs develop and are seeded through secondary particles produced by other RREAs (e.g., Dwyer, 2003, 2008; Skeltved et al., 2014). The system is triggered by an elevation of the electric field in a given region, presumably caused by an ascending lightning leader, along with cosmic ray secondary electrons acting as initial seeds. In lightning leader-based models, copious amounts of thermal runaway electrons are produced by the leader itself. The runaway electrons avalanche in the electric potential drop ahead of the lightning leader and possibly in the background electric field, if the latter is sufficiently strong to drive the acceleration of
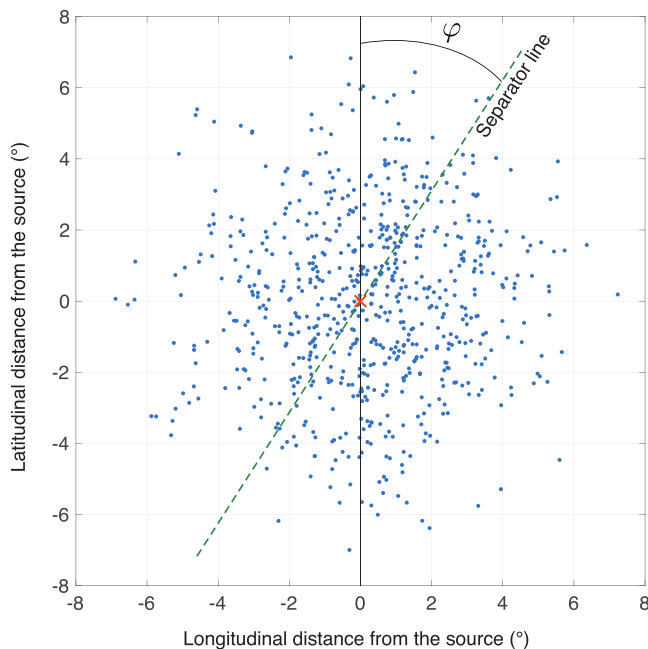
Figure 1. Locations of Fermi at the time of TGFs in the Fermi-GBM catalog relative to their WWLLN association in the horizontal plane. Here, the Fermi-GBM catalog is restricted to CTTE data. WWLLN sources are located at the origin and represented by a red cross. The separator line (dashed green line) is used to determine the probability that the excess in the number of TGFs lying on one side of the line compared to the number on the other side is due to random fluctuations (*p*-value). The azimuthal angle φ defines the orientation of the separator line.

runaway electrons (e.g., Carlson et al., 2010; Celestin et al., 2015; Dwyer, 2008; Moss et al., 2006). The seeding of high-energy electrons and the electric field magnitude in the source regions represent outstanding research questions in the understanding of TGFs.

In the context of atmospheric discharges, the effect of the geomagnetic field is usually neglected because of the high electron-molecule collision rates. The collision rate being typically higher than the cyclotron frequency, the electron distribution mostly remains isotropic, even in reduced air density, as, for instance, in the upper atmosphere (see Pasko et al., 1997). This is presumably the reason that the effect of geomagnetic field on RREAs has seldom been studied, with notable exceptions. Lehtinen et al. (1999) and Cramer et al. (2016) have quantified RREA rates in the presence of a magnetic field. From these papers, it can be seen that the strength of the geomagnetic field ($<50\,\mu$T) is not sufficient to have a significant effect on RREA rates. Babich et al. (2004) have investigated the role of the geomagnetic field on TGFs in the theoretical framework of high-altitude TGF production (>25 km), therefore associated with low absolute electric field magnitudes. These production altitudes are now believed to be inconsistent with TGF observations and their related radio emissions.

In the present work, we show that a statistically significant excess of TGFs detected to the east of their presumed lightning source is present in the recently established Fermi-Gamma-ray Burst Monitor (GBM) TGF catalog (Roberts et al., 2018). The discovered east-west asymmetry is quantitatively consistent with the expected RREA deviation from the geomagnetic field. We show how the deviation of RREAs by the geomagnetic field can be estimated analytically for homogeneous electric and magnetic fields in the acceleration region, and demonstrate the validity of this approach through comparison with numerical results. Finally, we present a method to infer the electric field in TGFs source regions through the obtained deviation of RREAs by the geomagnetic field.

2. Methods

2.1. Fermi-GBM, WWLLN Associations, and Geographical Asymmetry in the TGF Population

The GBM instrument on board Fermi is made of 12 thallium-doped sodium iodide (NaI(Tl)) and two bismuth germanate (BGO) detectors (Meegan et al., 2009). The BGO detectors cover an energy range from 200 keV to 40 MeV, while the NaI(Tl) detectors cover an energy range from 10 keV to 1 MeV. In the present work, we use the first Fermi-GBM TGF catalog (Roberts et al., 2018, and references therein), which contains 4,136 TGFs detected between Fermi's launch on 11 July 2008 through 31 July 2016. The catalog consists of TGFs identified using online and off-line searches. The online search is autonomously performed on spacecraft since launch, while the off-line search uses time-tagged event (TTE) data containing information on each single photon count received by the GBM detector. The off-line search started on 16 July 2010 and was based on downlinked TTE data corresponding to fractions of Fermi's orbit over active storm regions through 25 November 2012. Starting 26 November 2012, TTE data corresponding to full orbits are downlinked. This data collection is referred to as continuous TTE (CTTE). In the off-line search, specific detection criteria maximizing the number of TGFs and minimizing false positives are implemented (Briggs et al., 2013).

We make use of TGFs that have been time correlated with sferics detected from the World Wide Lightning Location Network (WWLLN) (e.g., Hutchins et al., 2012). In the Fermi-GBM catalog, a time window of ± 3.5 ms around the TGF detection time is used to define an association with a WWLLN sferic. Thus, 1,544 sferics from the WWLLN have been correlated with TGF events detected by Fermi-GBM. More information about TGFs in the Fermi-GBM catalog and the association procedure with WWLLN events can be found in Roberts et al. (2018). Several sferics of this ensemble may be associated with the same TGF event, in which case we

select the one closest in time to the TGF. We end up with 1,341 separate WWLLN-associated TGFs, which we will focus on in the present work. The sources of TGFs are considered to be located at the same position as their WWLLN match.

One of the goals of the present paper is to identify a possible asymmetry in the beaming of TGF photons that would be consistent with the deviation of RREAs by the geomagnetic field. Figure 1 shows the position of TGFs detected by Fermi relative to their associated WWLLN-located source. At first glance, the TGFs seem to be distributed symmetrically about their presumed source (WWLLN location) in Figure 1, but a more careful analysis needs to be carried out to quantify the degree of anisotropy of TGF source directions. The azimuthal angle φ defining the orientation of the separator line used in this study (see Figure 1) varies from 0° to 360°. We wish to determine the extent to which the difference between the number of TGFs on one side of the separator line compared to the other side can be explained by random fluctuations for each angle. For each angle φ, we hence need to calculate the probability for a symmetric randomly distributed population of TGFs of the same size to produce an excess of TGFs equal to or higher than that present in the data. For each azimuthal angle φ, we calculate a *p*-value through a binomial cumulative distribution function, under the null hypothesis that the TGF population does not present an excess greater than 50% on one side of the separator line (this side is taken as the east side when $\varphi = 0°$). Results are presented in section 3.1.

2.2. Deviation of RREAs in Homogeneous $(\overrightarrow{E}, \overrightarrow{B})$-Fields

The magnitude B of the geomagnetic field $\overrightarrow{B}$ is lower than ~50 µT for latitudes below 30° (e.g., Finlay et al., 2010), which encompasses Fermi's orbit. Cramer et al. (2016) have shown that the dynamics of RREAs (e.g., RREA rates, characteristic lengths, and speed) would not be significantly modified in such low magnetic fields. Moreover, the electric field threshold above which RREAs can develop is known to be $E_{\text{th}} = 2.8 \times N/N_0$ kV/cm (e.g., Dwyer et al., 2012), where N is the local air density and N_0 is the air density at ground level. As TGFs are believed to be associated with RREAs, the electron acceleration takes place in electric fields stronger than E_{th}. As TGF sources are thought to be generally located below 15 km altitude, the magnitude E of the local electric field $\overrightarrow{E}$ in which TGF-causative electrons accelerate is greater than 0.42 kV/cm, which is greater than the speed of light c multiplied by the magnitude of the geomagnetic field $cB \simeq 0.15$ kV/cm; thus, $E > cB$. This situation is opposite to that leading to an $\overrightarrow{E} \times \overrightarrow{B}$ drift often encountered in space plasmas, which requires $E < cB$. As shown in Appendix A, the resulting electron dynamics in the $E > cB$ case is not a slow drift but a continuous acceleration with a tilt angle with respect to the electric field.

For the sake of clarity, the main results of Appendix A are summarized below. To solve the trajectory of relativistic electrons subjected to an $(\overrightarrow{E}, \overrightarrow{B})$-field, it is convenient to find an inertial frame of reference in which the magnetic field becomes small, or even negligible, hence drastically simplifying the equation of motion of electrons. Indeed, electrons would mainly accelerate in the electric field in that frame. It is insightful to write the two Lorentz invariant quantities formed from the electric and magnetic fields. Using the antisymmetric electromagnetic four-tensor $F_{\mu\nu}$ and its dual $F_{\mu\nu}^* = \frac{1}{2}\epsilon_{\mu\nu\rho\sigma}F^{\rho\sigma}$, where $\epsilon_{\mu\nu\rho\sigma}$ is the completely antisymmetric unit tensor of the fourth rank (with $\epsilon_{0123} = -1$) and where we made use of the Einstein summation convention, one can form two Lorentz invariants:

$$\frac{1}{2}c^2 F_{\mu\nu}F^{\mu\nu} = c^2 B^2 - E^2 \tag{1}$$

$$\frac{1}{2}c^2 F_{\mu\nu}^* F^{\mu\nu} = -2c\overrightarrow{B} \cdot \overrightarrow{E} \tag{2}$$

Because $E > cB$ is verified in one frame of reference, the fact that $c^2B^2 - E^2$ is invariant through Lorentz transformation (Equation 1) implies that $E > cB$ holds in any frame of reference. Equation 2 shows that if $\overrightarrow{E}$ and $\overrightarrow{B}$ are perpendicular in one frame of reference, $\overrightarrow{B} \cdot \overrightarrow{E} = 0$ in any frame of reference, and as $E > cB$, one can find one frame of reference in which $B = 0$ in that particular case. Conversely, if the magnetic and electric field vectors form an angle in one frame of reference, as $\overrightarrow{B} \cdot \overrightarrow{E} \neq 0$ is invariant, one cannot find a frame in which $B = 0$.
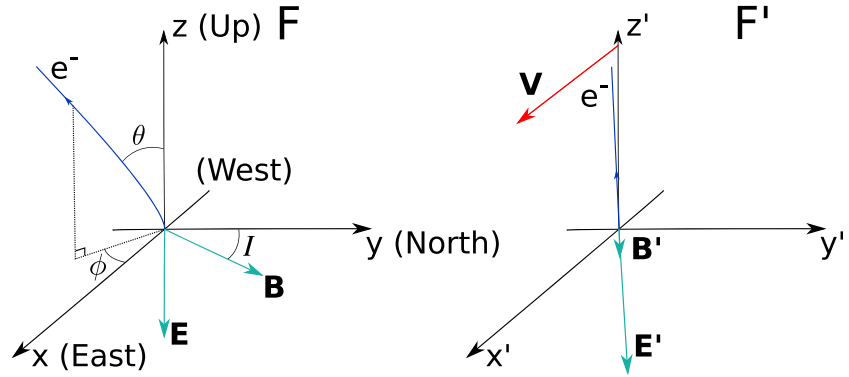
Figure 2. Illustration of the $(\vec{E}, \vec{B})$-fields in the frames of reference F (attached to the Earth) and F$'$ (in inertial motion of velocity $\vec{V}$ with respect to F). The electric field vector is assumed vertical, and the magnetic field vector is assumed to lie in the yOz plane. Considering $\vec{V} = c^2\dfrac{\vec{E} \times \vec{B}}{E^2}$, the magnetic field vector $\vec{B}'$ in F$'$ is vertical, and the direction of the electric field vector $\vec{E}'$ changes slightly given that $E > cB$ (see Appendix A). The resulting electron motion in F$'$ is mostly vertical.

In Appendix A, we show that using the particular frame of reference F′ in inertial motion with respect to the frame F attached to the Earth with a velocity $\vec{V} = c^2\dfrac{\vec{E} \times \vec{B}}{E^2}$, where $\vec{E}$ and $\vec{B}$ are the electric and magnetic field vectors in F, the influence of the magnetic field is small in F′, and the estimation of the electron motion in F′ is hence simplified (see Figure 2). The electric field vector is assumed to be vertical, and the magnetic field vector is assumed to lie in the yOz plane without any loss of generality as the coordinate system can always be rotated so that this condition is fulfilled. In F, one considers the polar angle θ formed between the electron velocity and the z-axis and the azimuthal angle ϕ between the projected velocity onto the horizontal plane (containing the x- and y- axes) and the x-axis (see Figure 2). We obtain the following relations (see Appendix A):

$$\sin\theta \simeq \frac{c\|\vec{E} \times \vec{B}\|}{E^2} \tag{3}$$

$$\sin\phi \simeq -\frac{c\vec{B} \cdot \vec{E}}{E^2} \tag{4}$$

In the present work, VLF measurements from WWLLN were used to geolocate the Fermi-GBM TGF sources. The local geomagnetic field vector is estimated at each source location using a MATLAB implementation by Compston (2019) of the eleventh generation of the International Geomagnetic Reference Field (IGRF) model (Finlay et al., 2010). Once the magnetic field vector at a given TGF location is known, we assume an electric field vector (vertical or tilted) and determine the set of rotations to perform on the coordinate system so that $\vec{E}$ is vertical in the new coordinate system and $\vec{B}$ lies in the yOz plane. The procedure we use involves the determination of rotation matrices to be applied on $\vec{E}$ and $\vec{B}$. One needs to use two rotation matrices R_z and R_y, respectively, about the z- and y-axes, in order to place the vector $\vec{E} \times \vec{B}$ along the x-axis, and one rotation matrix R_x (about the x-axis) to rotate $\vec{E}$ and $\vec{B}$ so that $\vec{E}$ is placed along the z-axis. One defines the unit vector $\vec{\delta} = \dfrac{\vec{V}}{\|\vec{V}\|}$, named deviation vector hereafter. The deviation vector $\vec{\delta}_R$ can be calculated in the rotated coordinate system using Equations 3 and 4. Then, one can obtain the deviation vector $\vec{\delta}$ in the original coordinate system using the following transformation: $R_z^{-1}R_y^{-1}R_x^{-1}\vec{\delta}_R = \vec{\delta}$.

For the sake of simplicity, the electric field magnitude is obtained assuming an acceleration region where the electric field is purely homogeneous. This models a situation in which RREAs would produce most of the
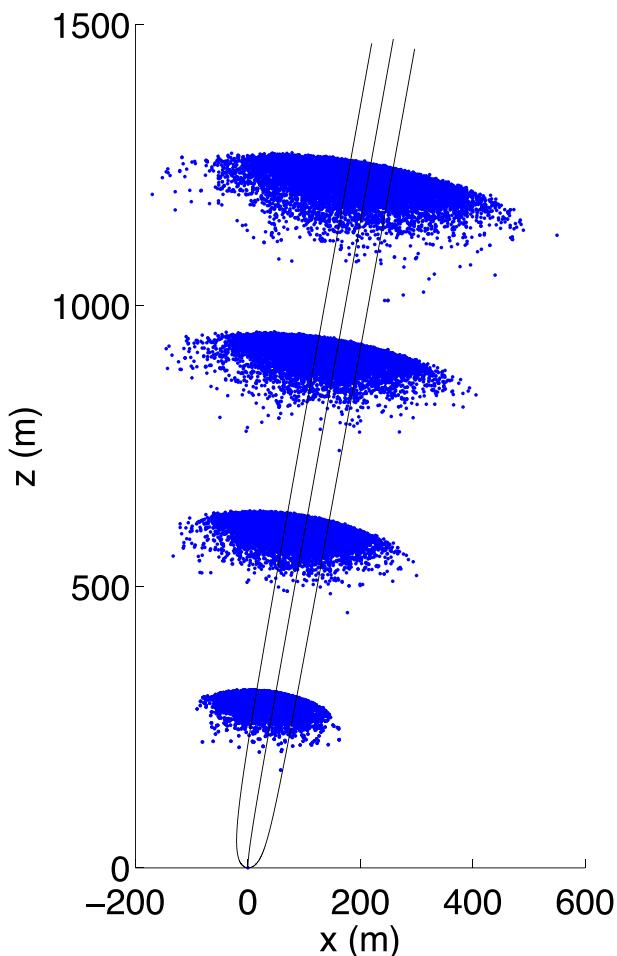
Figure 3. Blue dots show the positions of electrons (>1 keV) obtained using a Monte Carlo model every 1.07 μs in the case of a RREA propagating at an altitude of 15 km in a downward electric field of magnitude equal to two RREA thresholds and a magnetic field along the *y*-axis of magnitude 50 μT. Initial electrons propagate upward with an initial energy of 1 MeV. Solid black lines are electron trajectories obtained solving the relativistic equation of motion numerically accounting for a continuous friction. The three lines from left to right correspond to initial angles with respect to the *z*-axis of −90°, 0°, and 90°.

bremsstrahlung when developing in a large-scale thunderstorm electric field (were the seed runaway electrons to be produced by a lightning leader or relativistic-feedback processes). We have compared the analytical results reported here with Monte Carlo simulations taking into account every single electron collision and found that they match to a high degree of accuracy. For instance, Figure 3 shows the positions of electrons (>1 keV) at moments of time separated by steps of 1.07 μs obtained using a Monte Carlo model in the case of a RREA propagating at an altitude of 15 km in a downward electric field of magnitude equal to two RREA thresholds and a magnetic field along the *y*-axis of magnitude 50 μT.

The effect of the magnetic field is implemented through a relativistic Boris algorithm (Birdsall & Langdon, 1985). Also shown in Figure 3 are electron trajectories estimated by numerically solving the relativistic equation of motion for electrons accounting for a continuous friction. This model uses the same particle mover as that in the Monte Carlo code but assuming a continuous dynamic friction calculated through the Bethe formula with a mean excitation potential of 85.7 eV, which is representative of air (e.g., ICRU Report 37, 1984, Table 3.1). The magnetic deviation calculated using Equation 3 matches that obtained by solving the continuous equation of motion numerically perfectly, and both are close to Monte Carlo modeling results.

Thus, as the geomagnetic field points mostly northward, one can expect a systematic eastward deviation of TGFs. While the electric field orientation is likely to change significantly from one event to the other, opposite orientations should cancel out, whereas the magnetic eastward deviation is always present. Significant magnetic deviation should also be present in highly inhomogeneous electric fields produced by lightning leaders (Celestin, 2016, 2018), but this is beyond our scope here. Note that it is possible that other mechanisms (e.g., meteorological) would lead to other systematic deviations of runaway electron beams acting in addition to the deviation discussed here. In principle, those processes might also be distinguishable statistically (see section 4).

2.3. Photon Transport

After the deviation of the electron beam is quantified, it is important to take into account the photon transport in the atmosphere to model a given population of TGFs. Indeed, due to the reduced amount of atmosphere along a vertical line, photons escape to space preferentially vertically, which modifies the deviation of observed TGFs as compared to what would be expected if the effect of the atmosphere was negligible, that is, for a deviation caused by the tilt of the electron beam alone.

To model this effect, we use a Monte Carlo code simulating the transport of high-energy photons through the atmosphere. The model is similar to that presented in Østgaard et al. (2008). Three types of collisional processes are taken into account, namely, photoelectric absorption, Compton scattering, and electron-positron pair production. Using this model, we calculate the mean location of photons at Fermi's altitude. We estimate the effect of the atmosphere on the mean deviation of photons escaping to space for the beam angles (opening half angles) 30° and 45° (e.g., Carlson et al., 2007; Gjesteland et al., 2011; Mailyan et al., 2016; Xu et al., 2012), inside which photons are isotropically distributed. Beams are tilted with respect to the vertical axis by steps of 5°. These simulation runs were used to generate a lookup table from which the correspondence between electron beam deviation and mean location of photons at satellite altitude is read (see Figure 4).

We linearly interpolate the values contained in this lookup table for any tilt angles. The general effect of the atmospheric density gradient is as follows. For a photon beam with opening half angle of 45°, the mean
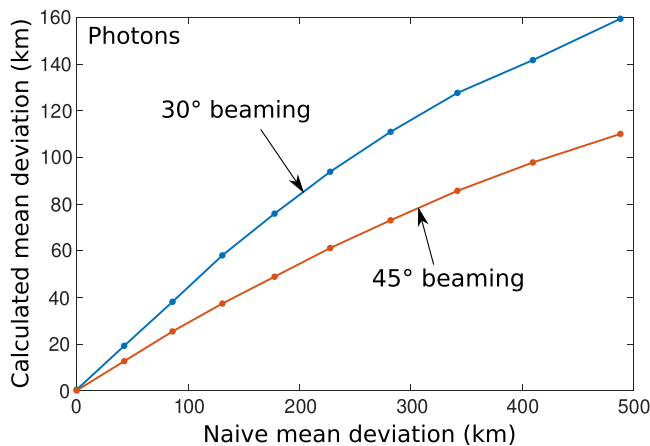
Figure 4. Mean deviation of photons at 500 km altitude as a function of the mean deviation assuming that the effect of the atmosphere is negligible (hence referred to as "naive") calculated using a photon transport Monte Carlo model assuming a source at 12 km. Results are presented for two beaming geometries.

location of the population of photons at a given low-orbit altitude is approximately one fourth of the mean location of unscattered photons (which location is aligned with the electron beam axis) for tilt angles between 0° and 45° from the vertical axis. For a photon beam with an opening half angle of 30°, the reduction in the mean deviation of photons due the presence of the atmosphere as compared to what would be expected is reduced to approximately a third. Although a uniform distribution in solid angle of the photon beam is often assumed in the literature, different angular distributions, but also source altitudes, and possibly correlated intrinsic brightness, might introduce some variation of the results presented in Figure 4. These are clearly some of the aspects in which the general method presented in this paper can be refined.

3. Results

3.1. East-West Asymmetry

Figure 5 shows the p-value under the null hypothesis that the TGF population does not present an excess greater than 50% on one side of the separator line (this side is taken as the east side when $\varphi = 0°$) for various angles φ (Figure 1). In other words, it shows the probability that a symmetric random population of TGFs would present a larger or equal number of TGFs on one side of the separator line to that of the observed TGF population, as a function of φ (see section 2.1). Figure 5a is a polar diagram of this p-value for all the TGFs with WWLLN associations in the Fermi-GBM catalog. It is clear that the lowest probability is reached for $\varphi \simeq 0$, which corresponds to an overpopulation of TGF detections in the east, as would be expected in the case where upward electron beams are deviated by the geomagnetic field.

Because of its orbit, Fermi has an increased exposure time per unit area close to the highest latitudes reached ($\sim \pm 26°$) (e.g., Briggs et al., 2013). This feature, correlating with the irregular geography of the Earth, enhanced with the fact that TGFs are known to occur more likely in coastal regions (e.g., Briggs et al., 2013; Smith et al., 2010), may introduce a source-to-satellite north-south bias in the satellite observation data. In order to correct for this bias, we use a subset of the Fermi TGF catalog, which corresponds to satellite locations well within the orbit's extreme latitudes, namely, within $\pm 16°$ latitude (i.e., about 1,100 km within the latitude boundaries). Similarly, Fermi-GBM is turned off over a region encompassing the South Atlantic Anomaly (SAA), the boundaries of which would introduce a complicated source-to-satellite geometry bias. We hence choose to exclude a greater region encompassing the SAA, corresponding to longitudes ranging from $-116°$ to $0°$ for latitudes $<5°$. Additionally, for the same reason as with the SAA exclusion zone, since previous TGFs observed by Fermi occurred over a selected area (TTE data), we only consider CTTE data in this TGF subset. Figure 5b shows the estimated p-value for the corresponding TGF subset that comprises 614 TGFs. One can see that the east-west asymmetry is even more clearly pronounced than in Figure 5a.

Figure 5c shows the same data as those displayed in Figures 5a and 5b but in a semilog plot. It can be seen that for all 1,341 TGFs with WWLLN associations in the Fermi-GBM catalog, as well as for the selected subset of 614 TGFs that are well within the orbit boundaries, the probability that the source-to-satellite asymmetry is uniquely explained by random fluctuations is lowest close to the west-to-east direction ($\varphi \simeq 0$). For both TGF ensembles studied here, this probability reaches values lower than 0.05. For the selected TGF subset the p-value is lower than 1/1,000 in the eastward direction. It is also interesting to note that apart from azimuthal angles close to $\varphi \simeq 0$, p-values are around the 0.5 level, showing that no preferred detection orientation is found apart from the eastward direction. Independently of the exact mechanisms causing it, the eastward detection excess can hence be deemed statistically significant for TGFs in the Fermi-GBM catalog.

However, it is important to note that care should be taken when trying to interpret the exact shape of the results presented in Figure 5. Clearly, strong correlations would be present from one angle φ to the next and, in the present paper, we do not try to make too much sense of the particular shapes of polar diagrams in Figures 5a and 5b.
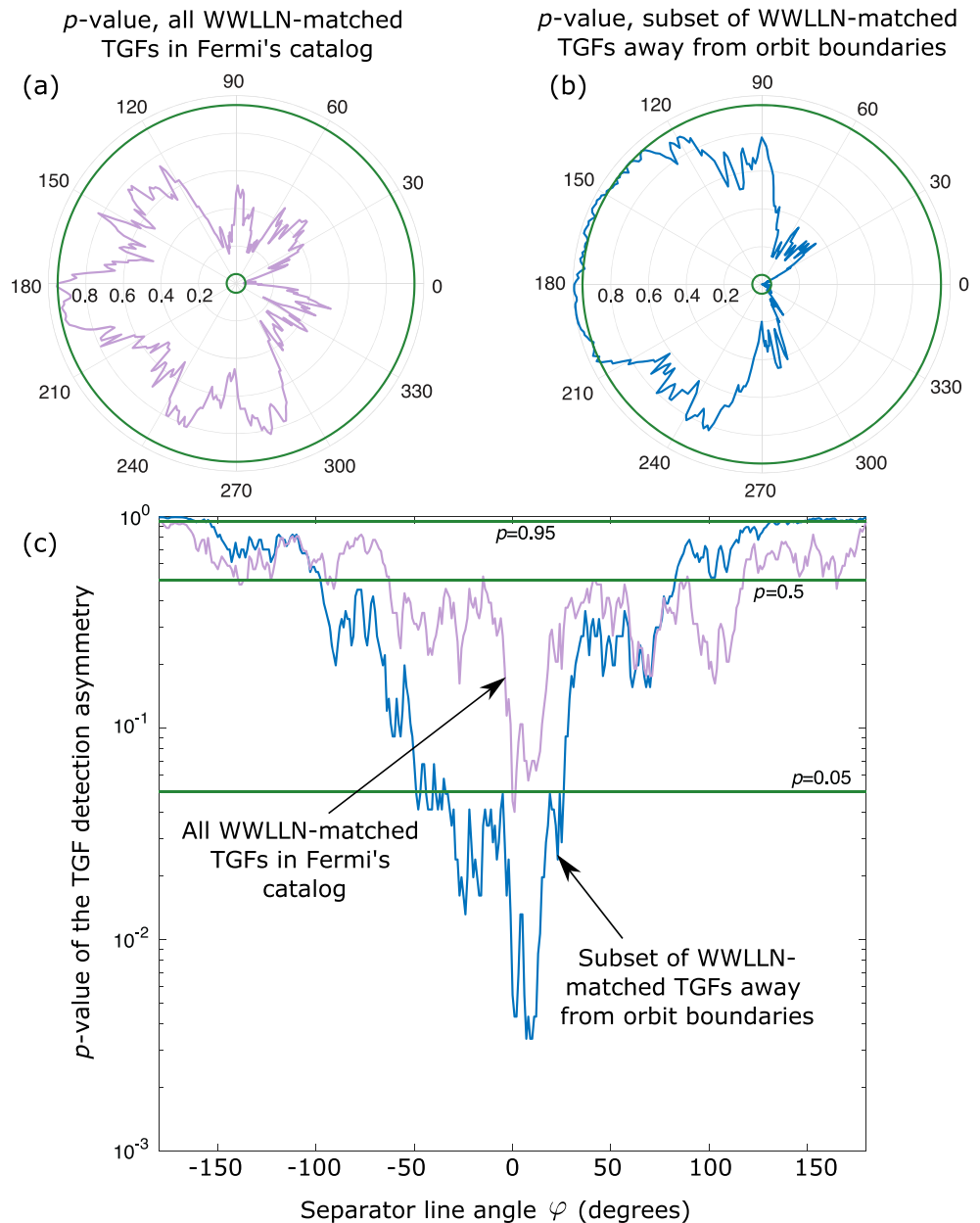
Figure 5. The *p*-value under the null hypothesis that the TGF population does not present an excess greater than 50% on one side of the separator line (this side is taken as the east side when $\varphi = 0°$) (see Figure 1). Panels (a) and (b) are polar diagrams showing the *p*-value as a function of the azimuthal angle φ. All 1,341 TGFs with WWLLN associations in Fermi-GBM catalog are included in panel (a). In panel (b), a selected subset of 614 TGFs with WWLLN associations that are well within the orbit boundaries is used. This subset is used in an attempt to reduce source-to-satellite observation geometry biases caused by the variable exposure time and the coastline geometry close to orbit boundaries. Panel (c) shows the data displayed in panels (a) and (b) in a semilog plot. The green lines represent the levels $p = 0.05$ and $p = 0.95$. We also show the level $p = 0.5$ in panel (c).

3.2. Mean Eastward Deviation

Beside the statistical significance of the excess of TGFs detected to the east of their sources, one can calculate the average longitudinal or latitudinal distances between TGF sources and Fermi at the moment of the detection. Considering all 1,341 TGFs with WWLLN associations in the Fermi-GBM catalog, one obtains a mean longitudinal distance of 0.0447° and a mean latitudinal distance of −0.0217°, corresponding to

Table 1
Statistical Properties of the Source-to-TGF Geometry for the Two TGF Ensembles Studied in This Paper

TGF ensemble type		Mean (CI)[a]	Median (CI)	Standard deviation (CI)
All 1,341 WWLLN-matched TGFs in Fermi-GBM catalog	Latitudinal distance	−0.0217°(±0.131)	−0.0046°(±0.180)	2.452°(±0.098)
	Longitudinal distance	0.0447°(±0.124)	0.0790°(±0.129)	2.312°(±0.088)
Subset of 614 WWLLN-matched TGFs	Latitudinal distance	0.0529°(±0.196)	0.0825°(±0.259)	2.481°(±0.139)
	Longitudinal distance	0.201°(±0.187)	0.274°(±0.244)	2.357°(±0.133)

[a]CI: 95% confidence level interval.

distances of 5.4 and −2.6 km at low-orbit altitude, respectively. For the 614-TGF subset, one gets a mean longitudinal distance of 0.201° and a mean latitudinal distance of 0.053°, corresponding to 24.4 and 6.4 km at low-orbit altitude (565 km), respectively. These values are summarized in Table 1 along with their 95% confidence level interval (CI).

Because the inner boundaries associated with the SAA can produce strong east-west biases in the data (see section 3.1), the mean deviation is calculated using the 614-TGF subset in the present work.

3.3. Inferring the Electric Field Magnitude in the TGF Source Region

Following the method presented in section 2.2, in a first step, we fix the magnitude of the electric field for every TGF in the subset. As the direction of the electric field is believed to be highly variable (Lyu et al., 2016; Mailyan et al., 2019; Xu et al., 2019), random directions of downward electric field vectors within 45° about the vertical axis are then defined for each TGF. The specific choice of limit angle has little effect on the final results (see section 4). The geomagnetic field vector is estimated at each TGF-associated WWLLN location using the IGRF model. From the knowledge of the electric and magnetic field vectors, one calculates the deviation of each TGF axis analytically (section 2.2) while taking into account the air density gradient effect (section 2.3) and the altitude of Fermi at the moment of the detection.

We repeat this procedure sweeping electric field magnitudes over a range from $E \simeq 2 \times 10^4$ to 2.6×10^5 V/m. In the context of TGFs, it is convenient to think of electric field magnitudes in terms of ratios to the RREA threshold, which depends on the altitude. For the sake of clarity, we hence discuss the electric field values in terms of the ratio $\xi = E/E_{th}$, where E_{th} is the RREA threshold at an altitude of 12 km, which is believed to be well in the range of TGF source altitudes (see section 1). The range of electric field magnitudes studied here exactly covers $\xi = 0.3$ to 4, with a step of 0.4. In order to quantify the variability of the results given by the random directions of electric field vectors, we repeat this procedure 1,000 times for each field magnitude.

Figure 6 shows the results for an assumed isotropic TGF beaming geometry within a 30° half-angle cone. Comparisons between Fermi's data and simulated populations of TGFs show that mean and median latitudinal deviations are consistent for any electric field magnitudes. However, the mean and median longitudinal distances are consistent only for a selected range of electric field magnitudes, namely, $\xi = 1.35 \pm 0.38$ for the mean and $\xi = 1.07 \pm 0.36$ for the median. It is important to note that uncertainties associated with statistical measures on Fermi's data (see Table 1) are large and discussed in the next section. We emphasize that they are not included in the reported estimates of the electric field ξ as those are modeling uncertainties.

4. Discussion

From this study, we cannot exclude that the significant eastward detection excess found would be produced by other effects than the deviation of RREAs by the geomagnetic field. For example, one could imagine that wind shears would systematically shift the charge layers in thunderstorms, bending the electric field vector in the source regions in such a way as to produce the observed data. In that case, it is however unclear how the electric field would end up in exactly this direction, as well as somehow being tuned to yield an effect so close to the effect expected assuming the geomagnetic deviation of RREAs. Nevertheless, at the present moment, we cannot rule out that the observed eastward TGF detection excess would be partly caused by a
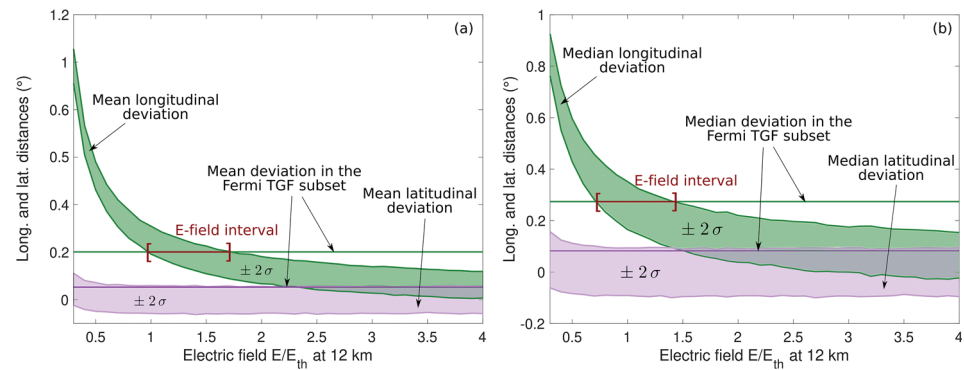
Figure 6. (a) Mean and (b) median longitudinal and latitudinal source-to-satellite distances of TGF photons obtained for random electric field directions and shown within two standard deviations as a function of the magnitude of the electric field. An isotropic TGF beaming geometry within a 30° half-angle cone is assumed. Shaded areas represent data-driven simulation results, while horizontal lines are calculated from Fermi's data. The electric field magnitude obtained using the mean corresponds to $\xi = 1.35 \pm 0.38$, while that obtained using the median is $\xi = 1.07 \pm 0.36$. Uncertainties associated with statistical measures on Fermi's data (see Table 1) are discussed in section 4.

systematic tilt of the space charge in thunderclouds, which would act in addition to the geomagnetic effect discussed here. It should however be possible to eliminate the possibility of other causes by exploring statistical deviations in different geographical regions with different magnetic field directions and magnitudes.

As part of a preliminary work, we have verified that a modification of the half angle of the cone restricting the directions of electric field vectors (chosen as 45° in this study) leads to a weak variation in the final results. However, the effect of the beaming angle of TGF source photons is more significant. The geometry of TGF source photon beams is not well known, and spectral study on individual TGFs indicates that some events are narrow, while others are wide (Mailyan et al., 2019). In the literature, the general agreement seems to be that TGF beaming geometries can be represented by photons distributed within a 30° to 45° half-angle cone (e.g., Carlson et al., 2007; Gjesteland et al., 2011; Mailyan et al., 2016; Xu et al., 2012). In this paper, we choose two limit cases, namely, 30° and 45° half-angle cones, and for the sake of simplicity, the distribution of photon momenta is assumed isotropic within that cone. The results presented in Figure 6 are obtained assuming TGF source photons are isotropically distributed within a 30° half-angle cone. A beam within a 45° half-angle cone leads to estimates of electric field magnitudes of $\xi = 0.90 \pm 0.17$ and $\xi = 0.66 \pm 0.14$, respectively, using the mean and median longitudinal distances in our TGF subset. The uncertainty reported here is smaller than that in the 30°-half-angle cone case mainly because the modeled deviation is lesser while the general shape of the $\pm 2\sigma$ range keeps close to that shown in Figure 6.

The uncertainties reported on the measured electric field amplitude in the previous parts of this paper are estimated based on the variability of the simulation results due to random directions of electric field vectors within a 45° half-angle downward cone (for one given magnitude). To complete the estimation of the electric field magnitude, one should also try to evaluate the confidence one has on the mean and median source-to-satellite distances in Fermi's data. Table 1 shows that the 95% confidence interval of the longitudinal distance for the mean and median are $\pm 0.187°$ and $\pm 0.244°$, respectively. These confidence intervals show that significant variations of the estimates reported here can be expected when using this method in the future. The confidence intervals will however reduce when considering larger sets of TGFs, from either not yet cataloged Fermi TGFs (i.e., detected after 31 July 2016) or other TGFs observed by other spacecraft.

In principle, the exclusion of TGFs near the north and south boundaries of Fermi's orbit (section 3.1) only removes asymmetry biases caused by the orbit in the north-south direction. These excluded TGFs should therefore be meaningful in terms of east-west deviation expected to be caused by the geomagnetic field. We chose to exclude them to demonstrate that only eastward excess is statistically significant (Figure 5b). Including these TGFs (hence only excluding a zone around the SAA) would make a subset of 904 TGFs, from which we find a mean west-to-east longitudinal deviation of 0.12° within a 95% confidence interval
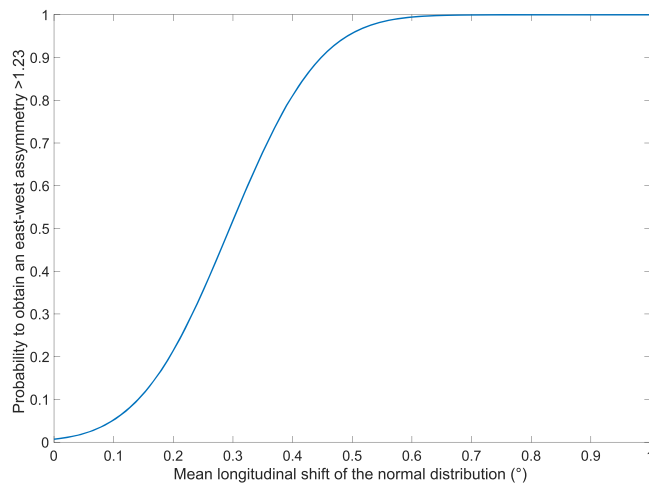
Figure 7. Estimated probability to obtain a population of 614 longitudinal distances with an east-west asymmetry >1.23 when drawn from a normal distribution with standard deviation 2.36° as a function of the mean longitudinal shift of that normal distribution.

[−0.03,0.27]. As expected, this confidence interval is smaller by a factor of about $\sqrt{904/614}$. Applying the same method as described in section 2.2, we find an estimate for the electric field of $\xi = 2.35 \pm 0.91$.

It is interesting to note that the distribution of source-to-satellite longitudinal distances of TGFs can be fit by a normal distribution with a standard deviation of 2.36° (see Table 1). Assuming that TGF deviations would only produce a longitudinal shift in this normal distribution, one can quantify the probability to obtain at least the observed asymmetry A (defined as the ratio of the number of TGFs detected from the east to the number of TGFs detected from the west) for various mean longitudes of the normal distribution. In the 614-TGF subset, one has $A \simeq 1.23$. Assuming mean longitudinal shifts varying from 0° to 1° by step of 0.01°, one draws one million random sets of 614 TGFs longitudinal distances from the satellite following a normal distribution with standard deviation 2.36°. In this way, we can estimate the probability to obtain an asymmetry greater than A.

Figure 7 shows this probability as a function of the eastward longitudinal shift assumed for the normal distribution. One can see that for a normal distribution of TGF longitudes with a longitudinal shift of 0.1°, the probability to obtain the asymmetry observed in the data is only ∼0.05. From this, we conclude that the true mean source-to-satellite longitudinal deviation is very likely to be greater than 0.1°.

It must be noted that east-west biases could also be rooted in the lightning localization data. Abarca et al. (2010) provide elements about WWLLN east-west biases based on their own work and several earlier papers. Previous papers report westward biases, while others report eastward biases. The average east-west bias is lower than the effect reported here with the 614-TGF subset. For instance, Abarca et al. (2010) report a westward localization bias of approximately 5 km over the contiguous United States. Systematic westward lightning localization biases would make TGFs look as if they were deviated eastward, as obtained in the present study. Projecting the mean TGF eastward deviation obtained here (0.201°) to the ground, we find a distance of approximately 22 km, albeit with a very large confidence interval (Table 1). However, as mentioned above, the mean longitudinal eastward deviation is likely >0.1°, which corresponds to >11 km on the ground, which also largely exceeds the reported lightning localization bias. Additionally, Abarca et al. (2010) also find a mean northward bias of about 4 km, which is close to their westward bias, while in the present study, we show that the TGF latitudinal deviation is much smaller than the longitudinal deviation. Although further investigation is necessary to include lightning localization biases using the general method introduced in the present paper, we conclude that the eastward TGF deviation reported here cannot be entirely explained by WWLLN lightning systematic localization error.

We emphasize that the geomagnetic effect is significant in our simulation results (see section 2.2). Therefore, if all the statistical source-to-satellite longitudinal deviation were to be caused by a systematic error in the lightning localization data, one would have to conclude that the electric field in TGF source regions is much greater than previously anticipated.

5. Conclusions

The main conclusions of this work may be summarized as follows:

1. A statistically significant excess of TGFs detected to the east of their presumed sources is present in the Fermi-GBM TGF catalog. It is the only significant source-to-satellite geometrical asymmetry we could find in the data.
2. This deviation is consistent with the expected effect of the geomagnetic field on relativistic runaway electron beams at ∼12 km altitude.
3. Based on the geomagnetic deviation, we have developed a method to estimate the magnitude of the electric field in TGF source regions, under the assumption that the electric field is homogeneous in these regions.

4. The electric field magnitudes we obtain are relatively strong and consistent with TGF production processes based on RREAs.

As a concluding remark, the results presented in this paper can be improved using a greater number of TGF observations, for example, from CGRO, RHESSI, AGILE, Fermi, and newer space missions dedicated to the observation of TGFs that have the capability to locate TGF sources using onboard optical cameras (e.g., ASIM and TARANIS) or X-ray imagers (ASIM).

Appendix A: Calculating the Deviation of Relativistic Electrons in Homogeneous $(\vec{E}, \vec{B})$-Fields Such That $\|\vec{E}\| > c\|\vec{B}\|$

The components of the electromagnetic field four-tensor $F_{\mu\nu}$ in covariant form can be written as

$$F_{\mu\nu} = \begin{bmatrix} 0 & E_x/c & E_y/c & E_z/c \\ -E_x/c & 0 & -B_z & B_y \\ -E_y/c & B_z & 0 & -B_x \\ -E_z/c & -B_y & B_x & 0 \end{bmatrix} \tag{A1}$$

We make use of Lorentz boosts to reduce the magnetic field and hence simplify the equation of motion in a given inertial frame (see below); it is thus interesting to note that two Lorentz invariants can be formed through $F_{\mu\nu}$. Note that in the following, we implicitly use the Einstein summation convention. Using $F_{\mu\nu}$ and its dual $F_{\mu\nu}^* = \frac{1}{2}\epsilon_{\mu\nu\rho\sigma}F^{\rho\sigma}$, where $\epsilon_{\mu\nu\rho\sigma}$ is the completely antisymmetric unit tensor of the fourth rank (with $\epsilon_{0123} = -1$), one obtains the two Lorentz invariants:

$$\frac{1}{2}c^2 F_{\mu\nu}F^{\mu\nu} = c^2 B^2 - E^2 \tag{A2}$$

$$\frac{1}{2}c^2 F_{\mu\nu}^* F^{\mu\nu} = -2c\vec{B}\cdot\vec{E} \tag{A3}$$

Considering a frame of reference F′ in inertial motion with velocity $\vec{V}$ with respect to the frame F (attached to the Earth), the application of the Lorentz transformation matrix $\Lambda^{\mu'}{}_{\mu}$ to the electromagnetic tensor expressed in the frame F leads to the electric and magnetic components in F′:

$$F^{\mu'\nu'} = \Lambda^{\mu'}{}_{\mu}\Lambda^{\nu'}{}_{\nu}F^{\mu\nu} \tag{A4}$$

Using Equation A4, the components of $F^{\mu'\nu'}$ can be written explicitly in terms of parallel and perpendicular components with respect to $\vec{V}$:

$$\vec{E_{\parallel}}' = \vec{E_{\parallel}} \tag{A5}$$

$$\vec{B_{\parallel}}' = \vec{B_{\parallel}} \tag{A6}$$

$$\vec{E_{\perp}}' = \gamma(\vec{E_{\perp}} + \vec{V} \times \vec{B}) \tag{A7}$$

$$\vec{B_{\perp}}' = \gamma\left(\vec{B_{\perp}} - \frac{1}{c^2}\vec{V} \times \vec{E}\right) \tag{A8}$$

where γ is the Lorentz factor.

One would like to find $\vec{V}$ so that the equation of motion of an electron becomes as simple as possible in F′. If $\vec{E}$ and $\vec{B}$ are perpendicular, i.e., $\vec{E} \cdot \vec{B} = 0$, the Lorentz invariant defined in Equation A3 shows that it should be possible to find F′ such that $B' = 0$ or $E' = 0$. Since $E > cB$ in F (see section 2.2), the invariant defined by Equation A2 is positive, and it is thus possible to find a frame in which $B' = 0$ if $\vec{E} \cdot \vec{B} = 0$. The dynamics of an electron in F′ would then be simply determined by the presence of the electric field

$\overrightarrow{E}{}'$. However, Equation A3 also shows that it is not the case for an arbitrary orientation of $\overrightarrow{E}$ and $\overrightarrow{B}$. Indeed, if $\overrightarrow{E}$ and $\overrightarrow{B}$ are not perpendicular in F, the invariance of $\overrightarrow{E} \cdot \overrightarrow{B}$ implies that none of the fields will cancel out in any inertial frames. We show below that it is still possible to minimize the effect of $\overrightarrow{B}{}'$, setting $\overrightarrow{V}$ as

$$\overrightarrow{V} = c^2 \frac{\overrightarrow{E} \times \overrightarrow{B}}{E^2} \tag{A9}$$

In that case, one sees that $\overrightarrow{E_\parallel} = 0$, $\overrightarrow{B_\parallel} = 0$, $\overrightarrow{E_\perp} = \overrightarrow{E}$, and $\overrightarrow{B_\perp} = \overrightarrow{B}$. From Equation A8, one gets

$$\overrightarrow{B_\perp}{}' = \overrightarrow{B}{}' = \gamma\left(\overrightarrow{B} - \frac{\overrightarrow{E} \times \overrightarrow{B}}{E^2} \times \overrightarrow{E} \right) = \gamma \frac{\overrightarrow{E} \cdot \overrightarrow{B}}{E^2}\overrightarrow{E} \tag{A10}$$

Equation A10 shows that, in the case $E > cB$ with perpendicular $\overrightarrow{E}$ and $\overrightarrow{B}$ fields, when using a velocity for F′ as defined in Equation A9, $\overrightarrow{B}{}'$ is perfectly canceled out. As was already noted in some classical textbooks (e.g., Jackson, 1975, Chap. 12.3), in that case, the motion of the electron is hyperbolic. A general formulation of the electron trajectories in static uniform electric and magnetic fields in any geometrical configurations can be obtained following, for instance, Jackson (1975, Problem 12.6) or Landau and Lifshitz (1994, Chap. 3 problem). However, the following original derivations pertain to the context of RREAs with typical magnetic and electric field magnitudes and capture the essential features of the electron motion in a simple way.

We consider $\overrightarrow{E} = -E\overrightarrow{e_z}$, and $\overrightarrow{B}$ in the yOz plane, that is, $\overrightarrow{B} = B_y\overrightarrow{e_y} + B_z\overrightarrow{e_z}$ (see Figure 2). The velocity $\overrightarrow{V}$ defined by the Equation A9 is therefore along the x-axis. As explained in section 2.2, there is no loss of generality implied by these assumptions as we rotate the coordinate system after the calculation of the deviation so as to place $\overrightarrow{E}$ and $\overrightarrow{B}$ in the desired position. Therefore, one obtains

$$\overrightarrow{B}{}' = -\gamma \frac{\overrightarrow{E} \cdot \overrightarrow{B}}{E}\overrightarrow{e_z} \tag{A11}$$

From Equation A7, one obtains

$$\overrightarrow{E_\perp}{}' = \overrightarrow{E}{}' = \gamma\left(\overrightarrow{E} + c^2\frac{\overrightarrow{E} \times \overrightarrow{B}}{E^2} \times \overrightarrow{B} \right) = \gamma\left[\overrightarrow{E}\left(1 - \frac{c^2 B^2}{E^2} \right) + c^2\frac{\overrightarrow{E} \cdot \overrightarrow{B}}{E^2}\overrightarrow{B} \right] \tag{A12}$$

Since $B < 50\,\mu$T and E is presumably greater than the RREA threshold field at the highest TGF altitude ($\sim$15 km), one has $\frac{c^2 B^2}{E^2} \ll 1$, and $\overrightarrow{E}{}'$ becomes

$$\overrightarrow{E}{}' \simeq \gamma\left(\overrightarrow{E} + c^2\frac{\overrightarrow{E} \cdot \overrightarrow{B}}{E^2}\overrightarrow{B} \right) = \gamma\overrightarrow{E} + \left(\gamma\frac{c^2 B}{E}\sin I \right)\overrightarrow{B} \tag{A13}$$

where, when the electric field is considered vertical, I is the inclination of the geomagnetic field at the considered location (Figure 2). In F′, the electric field can then be seen as consisting of two parts:

$$\overrightarrow{E}{}' \simeq \overrightarrow{E}{}'^{(0)} + \overrightarrow{E}{}'^{(1)} \tag{A14}$$

where $\overrightarrow{E}{}'^{(0)} = \gamma\overrightarrow{E}$ and $\overrightarrow{E}{}'^{(1)} = \left(\gamma\frac{c^2 B}{E}\sin I \right)\overrightarrow{B}$. Since $\frac{c^2 B^2}{E^2}\sin I \ll 1$, $\overrightarrow{E}{}'^{(1)}$ is a corrective term in the second order of $\frac{cB}{E}$. In the case of RREAs between 10 and 15 km, while $E'^{(0)} \sim 10^5$–10^6 V/m, one has $E'^{(1)} \sim 10^3$ V/m. The electric field in F′ is then mostly in the same direction as the electric field in F, that is along the z-axis. It is then clear that in F′, most of the electron kinetic energy is along the z-axis.

Since $u'_x \simeq 0$, one has $\frac{u'_x V}{c^2} \sim \frac{u'_x B}{E} \ll 1$, and the relativistic composition laws for velocities leads to $u_x \simeq V$. As $E'^{(1)} \ll E'^{(0)}$, most of the electron motion in the xOy plane is in the x component. With $u \simeq c$, one obtains

$$\sin\theta \simeq \frac{u_x}{u} \simeq \frac{V}{c} = \frac{c\|\overrightarrow{E} \times \overrightarrow{B}\|}{E^2} \tag{A15}$$

Although most of the electron motion in the xOy plane is along the x-axis, there is a smaller component to the electron velocity along the y-axis. Indeed, using the relativistic composition laws for velocities, one has

$$\frac{u_y}{u_z} = \frac{u'_y}{u'_z} \simeq \frac{E'_y}{E'_z} = \frac{E'^{(1)}_y}{E'^{(0)}_z} = \frac{\gamma c^2 \frac{\overrightarrow{E} \cdot \overrightarrow{B}}{E^2} B_y}{-\gamma E} = -c^2 \frac{\overrightarrow{E} \cdot \overrightarrow{B}}{E^3} B \cos I \tag{A16}$$

As $u_z \simeq c$, one obtains $u_y \simeq -c^3 \frac{\overrightarrow{E} \cdot \overrightarrow{B}}{E^3} B \cos I$. One can characterize this feature using the angle ϕ between the projection of the velocity onto the xOy plane $u_H \simeq c \sin\theta = \frac{cB}{E} \cos I$ and the x-axis (see Figure 2). One obtains

$$\sin\phi = \frac{u_y}{u_H} \simeq -\frac{c\overrightarrow{B} \cdot \overrightarrow{E}}{E^2} \tag{A17}$$

The geomagnetic deviation of runaway electrons characterized by the Equations A15 and A17 has been compared against numerical simulations for various electric and magnetic field geometries with and without the inclusion of a dynamic friction. The angles obtained through these equations and simulation results are in excellent agreement.

In conclusion, we identified three particular features for the motion of electrons:

1. Most of the kinetic energy is upward in the antiparallel direction of $\overrightarrow{E}$.
2. The mostly northward geomagnetic field causes an eastward deviation of runaway electrons characterized by Equation A15.
3. A lesser southward deviation directly caused by the nonperpendicularity of $\overrightarrow{B}$ and $\overrightarrow{E}$ is characterized by Equation A17.

Data Availability Statement

All GBM data used in this paper are available online (at https://fermi.gsfc.nasa.gov/ssc/data/access/gbm/). The Fermi-GBM catalog is available online (at https://fermi.gsfc.nasa.gov/ssc/data/access/gbm/tgf/). In this work, we have used the MATLAB implementation of the International Geomagnetic Reference Field (IGRF) model implemented by Drew Compston and made available on the MATLAB Central File Exchange at https://www.mathworks.com/matlabcentral/fileexchange/34388-international-geomagnetic-reference-field-igrf-model (Retrieved 27 March 2019). The data used in figures and results of this paper are available online (at https://doi.org/10.6084/m9.figshare.c.4868787.v2).

References

Abarca, S. F., Corbosiero, K. L., & Galarneau, T. J. (2010). An evaluation of the Worldwide Lightning Location Network (WWLLN) using the National Lightning Detection Network (NLDN) as ground truth. *Journal of Geophysical Research*, *115*, D18206. https://doi.org/10.1029/2009JD013411

Babich, L. P., Il'kaev, R. I., Kutsyk, I. M., Kudryavtsev, A. Y., Roussel-Dupre, R. A., & Symbalisty, E. M. (2004). Analysis of atmospheric gamma ray bursts based on the mechanism of generation of relativistic electron avalanches. *Geomagnetism and Aeronomy*, *44*(2), 243–251 English.

Birdsall, C. K., & Langdon, A. B. (1985). *Plasma physics via computer simulation*. New York, NY, USA: McGraw-Hill Book Co.

Briggs, M. S., Fishman, G. J., Connaughton, V., Bhat, P. N., Paciesas, W. S., Preece, R. D., et al. (2010). First results on terrestrial gamma ray flashes from the Fermi Gamma-ray Burst Monitor. *Journal of Geophysical Research*, *115*, A07323. https://doi.org/10.1029/2009JA015242

Briggs, M. S., Xiong, S., Connaughton, V., Tierney, D., Fitzpatrick, G., Foley, S., et al. (2013). Terrestrial gamma-ray flashes in the Fermi era: Improved observations and analysis methods. *Journal of Geophysical Research: Space Physics*, *118*, 3805–3830. https://doi.org/10.1002/jgra.50205

Carlson, B. E., Lehtinen, N. G., & Inan, U. S. (2007). Constraints on terrestrial gamma ray flash production from satellite observation. *Geophysical Research Letters*, *34*, L08809. https://doi.org/10.1029/2006GL029229

Carlson, B. E., Lehtinen, N. G., & Inan, U. S. (2010). Terrestrial gamma ray flash production by active lightning leader channels. *Journal of Geophysical Research*, *115*, A10324. https://doi.org/10.1029/2010JA015647

Celestin, S. (2016). Effects of the geomagnetic field on the beaming geometry of TGFs. In *Abstract EGU2016-15528, EGU General Assembly, 17–22 April*, Vienna, Austria.

Celestin, S. (2018). Geomagnetic effects on the beaming geometry of TGFs. In *Abstract P-11-16, 16th International Conference on Atmospheric Electricity, 17-22 June*, Nara, Japan.

Celestin, S., Xu, W., & Pasko, V. P. (2015). Variability in fluence and spectrum of high-energy photon bursts produced by lightning leaders. *Journal of Geophysical Research: Space Physics*, *120*, 10,712–10,723. https://doi.org/10.1002/2015JA021410

Compston, D. (2019). International Geomagnetic Reference Field (IGRF) Model. MATLAB Central File Exchange https://www.math-works.com/matlabcentral/fileexchange/34388-international-geomagnetic-reference-field-igrf-model

Cramer, E. S., Dwyer, J. R., & Rassoul, H. K. (2016). Magnetic field modification to the relativistic runaway electron avalanche length. *Journal of Geophysical Research: Space Physics*, *121*, 11,261–11,270. https://doi.org/10.1002/2016JA022891

Cummer, S. A., Briggs, M. S., Dwyer, J. R., Xiong, S., Connaughton, V., Fishman, G. J., et al. (2014). The source altitude, electric current, and intrinsic brightness of terrestrial gamma ray flashes. *Geophysical Research Letters*, *41*, 8586–8593. https://doi.org/10.1002/2014GL062196

Cummer, S. A., Lu, G., Briggs, M. S., Connaughton, V., Xiong, S., Fishman, G. J., & Dwyer, J. R. (2011). The lightning-TGF relationship on microsecond timescales. *Geophysical Research Letters*, *38*, L14810. https://doi.org/10.1029/2011GL048099

Cummer, S. A., Lyu, F., Briggs, M. S., Fitzpatrick, G., Roberts, O. J., & Dwyer, J. R. (2015). Lightning leader altitude progression in terrestrial gamma-ray flashes. *Geophysical Research Letters*, *42*, 7792–7798. https://doi.org/10.1002/2015GL065228

Dwyer, J. R. (2003). A fundamental limit on electric fields in air. *Geophysical Research Letters*, *30*(20), 2055. https://doi.org/10.1029/2003GL017781

Dwyer, J. R. (2008). Source mechanisms of terrestrial gamma-ray flashes. *Journal of Geophysical Research*, *113*, D10103. https://doi.org/10.1029/2007JD009248

Dwyer, J. R., & Smith, D. M. (2005). A comparison between Monte Carlo simulations of runaway breakdown and terrestrial gamma-ray flash observations. *Geophysical Research Letters*, *32*, L22804. https://doi.org/10.1029/2005GL023848

Dwyer, J. R., Smith, D. M., & Cummer, S. A. (2012). High-energy atmospheric physics: Terrestrial gamma-ray flashes and related phenomena. *Space Science Reviews*, *173*, 133–196. https://doi.org/10.1007/s11214-012-9894-0

Finlay, C. C., Maus, S., Beggan, C. D., Bondar, T. N., Chambodut, A., Chernova, T. A., et al. (2010). International Geomagnetic Reference Field: The eleventh generation. *Geophysical Journal International*, *183*, 1216–1230. https://doi.org/10.1111/j.1365-246X.2010.04804.x

Fishman, G. J., Bhat, P. N., Mallozzi, R., Horack, J. M., Koshut, T., Kouveliotou, C., et al. (1994). Discovery of intense gamma-ray flashes of atmospheric origin. *Science*, *264*, 1313.

Gjesteland, T., Østgaard, N., Collier, A. B., Carlson, B. E., Cohen, M. B., & Lehtinen, N. G. (2011). Confining the angular distribution of terrestrial gamma ray flash emission. *Journal of Geophysical Research*, *116*, A11313. https://doi.org/10.1029/2011JA016716

Hutchins, M. L., Holzworth, R. H., Brundell, J. B., & Rodger, C. J. (2012). Relative detection efficiency of the World Wide Lightning Location Network. *Radio Science*, *47*, RS6005. https://doi.org/10.1029/2012RS005049

ICRU Report 37 (1984). Stopping powers for electrons and positrons: International Commission on Radiation Units and Measurements.

Jackson, J. D. (1975). *Classical electrodynamics* (2nd ed.). New York, NY: Wiley.

Landau, L. D., & Lifshitz, E. M. (1994). The classical theory of fields. Fourth revised English edition.

Lehtinen, N. G., Bell, T. F., & Inan, U. S. (1999). Monte Carlo simulation of runaway MeV electron breakdown with application to red sprites and terrestrial gamma ray flashes. *Journal of Geophysical Research*, *104*, 24,699–24,712. https://doi.org/10.1029/1999JA900335

Lu, G., Blakeslee, R. J., Li, J., Smith, D. M., Shao, X.-M., McCaul, E. W., et al. (2010). Lightning mapping observation of a terrestrial gamma-ray flash. *Geophysical Research Letters*, *37*, L11806. https://doi.org/10.1029/2010GL043494

Lyu, F., Cummer, S. A., Lu, G., Zhou, X., & Weinert, J. (2016). Imaging lightning intracloud initial stepped leaders by low-frequency interferometric lightning mapping array. *Geophysical Research Letters*, *43*, 5516–5523. https://doi.org/10.1002/2016GL069267

Mailyan, B. G., Briggs, M. S., Cramer, E. S., Fitzpatrick, G., Roberts, O. J., Stanbro, M., et al. (2016). The spectroscopy of individual terrestrial gamma-ray flashes: Constraining the source properties. *Journal of Geophysical Research: Space Physics*, *121*, 11,346–11,363. https://doi.org/10.1002/2016JA022702

Mailyan, B. G., Nag, A., Murphy, M. J., Briggs, M. S., Dwyer, J. R., Rison, W., et al. (2018). Characteristics of radio emissions associated with terrestrial gamma-ray flashes. *Journal of Geophysical Research: Space Physics*, *123*, 5933–5948. https://doi.org/10.1029/2018JA025450

Mailyan, B. G., Xu, W., Celestin, S., Briggs, M. S., Dwyer, J. R., Cramer, E. S., et al. (2019). Analysis of individual terrestrial gamma-ray flashes with lightning leader models and Fermi Gamma-Ray Burst Monitor data. *Journal of Geophysical Research: Space Physics*, *124*, 7170–7183. https://doi.org/10.1029/2019JA026912

Marisaldi, M., Fuschino, F., Labanti, C., Galli, M., Longo, F., Del Monte, E., et al. (2010). Detection of terrestrial gamma ray flashes up to 40 MeV by the AGILE satellite. *Journal of Geophysical Research*, *115*, A00E13. https://doi.org/10.1029/2009JA014502

Meegan, C., Lichti, G., Bhat, P. N., Bissaldi, E., Briggs, M. S., Connaughton, V., et al. (2009). The Fermi Gamma-ray Burst Monitor. *Astrophysical Journal*, *702*, 791–804. https://doi.org/10.1088/0004-637X/702/1/791

Moss, G. D., Pasko, V. P., Liu, N., & Veronis, G. (2006). Monte Carlo model for analysis of thermal runaway electrons in streamer tips in transient luminous events and streamer zones of lightning leaders. *Journal of Geophysical Research*, *111*, A02307. https://doi.org/10.1029/2005JA011350

Østgaard, N., Gjesteland, T., Stadsnes, J., Connell, P. H., & Carlson, B. (2008). Production altitude and time delays of the terrestrial gamma flashes: Revisiting the Burst and Transient Source Experiment spectra. *Journal of Geophysical Research*, *113*, A02307. https://doi.org/10.1029/2007JA012618

Pasko, V. P., Inan, U. S., Bell, T. F., & Taranenko, Y. N. (1997). Sprites produced by quasi-electrostatic heating and ionization in the lower ionosphere. *Journal of Geophysical Research*, *102*, 4529–4562. https://doi.org/10.1029/96JA03528

Pu, Y., Cummer, S. A., Lyu, F., Briggs, M., Mailyan, B., Stanbro, M., & Roberts, O. (2019). Low frequency radio pulses produced by terrestrial gamma-ray flashes. *Geophysical Research Letters*, *46*, 6990–6997. https://doi.org/10.1029/2019GL082743

Roberts, O. J., Fitzpatrick, G., Stanbro, M., McBreen, S., Briggs, M. S., Holzworth, R. H., et al. (2018). The first Fermi-GBM terrestrial gamma ray flash catalog. *Journal of Geophysical Research: Space Physics*, *123*, 4381–4401. https://doi.org/10.1029/2017JA024837

Skeltved, A. B., Østgaard, N., Carlson, B., Gjesteland, T., & Celestin, S. (2014). Modeling the relativistic runaway electron avalanche and the feedback mechanism with GEANT4. *Journal of Geophysical Research: Space Physics*, *119*, 9174–9191. https://doi.org/10.1002/2014JA020504

Smith, D. M., Hazelton, B. J., Grefenstette, B. W., Dwyer, J. R., Holzworth, R. H., & Lay, E. H. (2010). Terrestrial gamma ray flashes correlated to storm phase and tropopause height. *Journal of Geophysical Research*, *115*, A00E49. https://doi.org/10.1029/2009JA014853

Smith, D. M., Lopez, L. I., Lin, R. P., & Barrington-Leigh, C. P. (2005). Terrestrial gamma-ray flashes observed up to 20 MeV. *Science*, *307*, 1085. https://doi.org/10.1126/science.1107466

Stanley, M. A., Shao, X.-M., Smith, D. M., Lopez, L. I., Pongratz, M. B., Harlin, J. D., et al. (2006). A link between terrestrial gamma-ray flashes and intracloud lightning discharges. *Geophysical Research Letters*, *33*, L06803. https://doi.org/10.1029/2005GL025537

Xu, W., Celestin, S., & Pasko, V. P. (2012). Source altitudes of terrestrial gamma-ray flashes produced by lightning leaders. *Geophysical Research Letters*, *39*, L08801. https://doi.org/10.1029/2012GL051351

Xu, W., Celestin, S., Pasko, V. P., & Marshall, R. A. (2019). Compton scattering effects on the spectral and temporal properties of terrestrial gamma-ray flashes. *Journal of Geophysical Research: Space Physics*, *124*, 7220–7230. https://doi.org/10.1029/2019JA026941